Relationships between microstructure and transport properties in mortar containing recycled ceramic powder

Le Li [*a], Wenfeng Liu[a], Qinxi You[a], Mengcheng Chen[a], Qiang Zeng [†b], Chunsheng Zhou[c], and Mingzhong Zhang[d]

[a] *Department of Civil Engineering and Architecture, East China Jiao Tong University, Nanchang, 330013, P. R. China*

[b] *College of Civil Engineering and Architecture, Zhejiang University, Hangzhou, 310058, P. R.China*

[c] *Department of Civil Engineering, Harbin Institute of Technology, Harbin, 150090, P. R. China*

[d] *Department of Civil, Environmental and Geomatic Engineering, University College London, London, WC1E 6BT, UK*

[*] Corresponding author, Department of Civil Engineering and Architecture, East China Jiao Tong University, Nanchang, 330013, P. R. China, Email: liniannian15@163.com

[†] Corresponding author, College of Civil Engineering and Architecture, Zhejiang University, Hangzhou, 310058, P. R. China, Email: cengq14@zju.edu.cn

Abstract

Sustainable utilization of ceramic wastes in construction has gained increasing interest, but the microstructure and transport properties of ceramic-modified construction materials remain to be explored before in-situ engineering application. This paper presents an experimental study on microstructure, mechanical properties and transport properties of cement mortars containing different percentages of ceramic powders (CPs) up to 40%. Microstructure of CP-cement mortars was measured using mercury intrusion porosimetry, water vapor sorption isotherm and scanning electron microscopy techniques. Mechanical properties including compressive strength and flexural strength as well as transport properties including gas permeability and capillary sorptivity were measured. Results indicate that ceramic powder can greatly refine the pore structure of CP-cement mortars. Because of the homogenization and densification effects of ceramic powder on mortar matrices and interfacial transition zones, the compressive and flexural strengths of CP-cement mortars at 180 d are around 80 MPa and 10 MPa, respectively. Both gas permeability and capillary sorptivity decrease substantially as ceramic powder content increases and exhibit linear correlations with pore structure characteristics such as total porosity and critical pore size. Ceramic powder can lower the manufacture costs of concrete and obtain better durability. Therefore, ceramic powder can be considered as a promising supplementary material to develop sustainable and durable cement-based materials for future engineering applications.

Keywords: Ceramic powder; Mortar; Microstructure; Gas permeability; Sorptivity; Sustainability.

Nomenclature

APSD	accumulative pore size distribution	LF	limestone filler
C_3A	tricalcium aluminate	MIP	mercury intrusion porosimetry
C_4AF	tetracalcium aluminoferrite	OPC	ordinary Portland cement
CH	calcium hydroxide	PSD	pore size distribution
CP	ceramic powder	RH	relative humidity
C_2S/C_3S	bi/tricalcium silicate	SEM	scanning electronic microscope
C-S-A-H	calcium-silicate-alumina-hydrates	SG	slag
C-S-H	calcium-silicate-hydrate	SSA	specific surface area
DPSD	differential pore size distribution	WVSI	water vapor sorption isotherm
EDS	energy-dispersive X-ray spectroscopy	XRD	X-ray diffraction
FA	fly ash	XRF	X-ray fluorescence
ITZ	interfacial transition zone		

1 Introduction

Ceramics, made of mixing and heating of clay, feldspar and quartz, are processed for different applications in our daily life, such as tableware and decoration purposes. It has been indicated that about 25% of daily production of ceramic industry, around 13 million tonnes, becomes waste in China (Tan et al., 2011). More than 95% of this waste is not recycled in any effective means, and there is an expected increase in the amount of waste produced due to the higher demand of ceramics in human daily use. This waste occupies agricultural land and other nearby areas on one hand. On the other hand, cement industry is one of the major emitters of carbon dioxide, and the production of Portland cement accounts for 5-7% of the total man made emission (Oggioni et al., 2011; Geng et al., 2019). The electrical specific energy consumption of cement production is 118 kWh/t (Madlool et al., 2011), which dominatingly accounts for the electrical energy in concrete production (Nisbet et al., 2000). An effective way to reduce these negative aspects may be recycling and reuse of ceramic wastes as a supplementary construction material, like other industry wastes, including marble (Singh et al., 2017), mineral wool (Chen et al., 2019), red mud (Hu et al., 2018) and glass (Chen et al., 2019). This not only utilizes ceramic wastes in a positive manner, but also may improve material properties.

A value-added application of waste ceramics is feasible after grinding to fineness comparable to cement. Partially replacing cement by ceramic powder (CP) provides a sustainable solution to reuse the ceramic wastes. The 10% replacement of cement by CP indicates a decrease of 3.31% specific energy consumption in cement production (Li et al., 2020). De

Rojas et al. (2018) found that the reactive silicon dioxide content in CP accounts for over 25%. Huang et al. (2009) evaluated the feasibility of incorporating CP into pavement material and indicated that the dynamic modulus and tensile strength of asphaltic concrete are both improved. Samadi et al. (2015) reported that the mortar with 20% of cement replaced by CP has a higher compressive strength than the reference mortar at 7 d, due to the high amount of aluminium oxide (Al_2O_3) in CP that raises the early strength. Due to the different contents of active minerals, the strength rises at early ages induced by CP do not always occur. For example, a slow strength-rising behaviour has been reported for CP-modified concrete (Pacheco-Torgal and Jalali, 2011; El-Dieb and Kanaan, 2018; Aly et al., 2019; Li et al., 2020). However, the strengths can eventually rise upto (or even higher than) that of the neat cement concrete with sufficient curing (Pacheco-Torgal and Jalali, 2011; El-Dieb and Kanaan, 2018; Aly et al., 2019; Li et al., 2020).

Durability of structural concrete has been valued in the design and construction of civil engineering infrastructures (Gui et al., 2016). Since the onsets of most deteriorations in concrete are highly related to gas and/or water transport, the gas permeability and capillary sorptivity are two fundamental quantities: the gas permeability depicts the transport rate of gas phase in pore network of concrete (Dullien, 1992), while the capillary sorptivity reflects the transport rate of liquid phase in pores of concrete (Sabir et al., 1998). These two quantities are considered as the performance indicators of durability for cement-based materials (Li et al., 2015, 2018). Physically, penetration of gas or water through a porous medium requires connected pore networks providing percolation paths, and thus the pore structure of cement-based materials plays a critical role in their transport properties. Recently, great efforts

have been made to establish generalized links between transport properties and material microstructure (or pore structure) (Song and Kwon, 2007; Esen and Yilmazer, 2010, 2011; Zhang et al., 2018; Li et al., 2018). The trials on cement-based materials containing CPs, however, seem less than those containing other micro fillers like fly ash (Esen, 2010; Hu et al., 2018), silca fume (Leung et al., 2016; Esen and Orhan, 2016) and slag (Mehta and Siddique, 2018). That is probably due to that CP resource is not as abundant as those micro fillers. But in some areas with prosperous ceramic industry in China, for example, Jingdezhen, named as the capital of 'china', waste ceramics have massively stacked.

Exploring the transport properties of CP-modified concrete and the microstructure associations not only helps deepen the understandings in the chemico-physical regimes of mass transport and microstructure development in micro filler-cement system, but also provides strong bases for future engineering uses of CP. Cheng et al. (2016) measured the water permeation depth of concrete with 10-40% CP content, and found that a higher cement replacement ratio by CP induces a lower permeability. By contrast, Pacheco-Torgal and Jalali (2010) reported no relevant differences in oxygen permeability for the concretes with and without CP. The debates may come from the relatively poor understandings in the pore structure of cement-based materials with CP and its influences on the transport properties. The aims of this study are therefore (1) assessing the effect of CP on the gas permeability and water sorptivity of CP-modified mortars; (2) measuring the pore structure alterations of the mortars by multi-scale tests; (3) exploring the relationship between the pore structure and the durability performance.

In this work, waste ceramics from local factory were ground to micro CP (with the

mean size of 3.5 μm) and used as a partial substitute of cement up to 40% to prepare CP-cement mortars. The mechanical properties of the CP-cement mortars were evaluated through compressive/flexural strength tests. The durability performances of the mortars were assessed through the gas permeability and capillary sorptivity tests. The mortars' microstructure was tested by mercury intrusion porosimetry (MIP), water vapor sorption isotherm (WVSI), and scanning electron microscopy (SEM) techniques. The links between the transport properties and some characteristic pore parameters were then established and discussed in details. The economic and durability benefits of CP-modified concrete were assessed based on local market prices and resources. The main purpose of this study is to investigate the feasibility and benefits of using CP as a partial substitute of cement that may provide promising engineering perspectives in sustainable uses of ceramic wastes in the ceramic producing areas of China.

2 Experimental program

2.1 Materials

Locally available Portland cement (identical to ASTM type I 42.5) was used as the only binder in this study. The main oxides in the cement, from an X-ray fluorescence (XRF) test, include silica, alumina, calcium oxide and ferric oxide. The active mineral phases of the cement were analyzed as dicalcium dilicate (C_2S), tricalcium silicate (C_3S), tricalcium aluminate (C_3A) and tetracalcium aluminoferrite (C_4AF). The detailed chemical compositions, minerals and physical properties are given in Table 1.

Table 1: Chemical/mineral composition and physical properties of cement and ceramic powder.

Composition/properties		Cement	Ceramic powder
Chemical composition (%)	CaO	59.64	6.67
	SiO_2	20.47	61.72
	Al_2O_3	5.90	22.31
	Fe_2O_3	4.80	1.24
	MgO	2.74	0.65
	SO_3	2.08	0.07
	Na_2O(eq)	0.80	0.96
	K_2O	-	1.55
	Loss on ignition	1.97	3.96
Minerals (%)	C_2S	21.23	
	C_3S	56.59	
	C_3A	7.47	
	C_4AF	8.89	
Physical properties	Density (kg/m^3)	3100	2560
	Specific surface area (m^2/kg)	343	458
	Mean particle size (μm)	9.8	3.5

Figure 1: Ground ceramic preparation process: (a) raw ceramic products as received; (b) coarse ceramic particles ground by jaw crusher; (c) micro ceramic particles powdered by air jet mill.

The waste ceramics used in this study were supplied by a local ceramics enterprise in Jingdezhen, China. Those ceramic wastes mainly include broken decorative vases and flowerpots, and daily used bottles and bowls (Figure 1a). Compositional variance may exist in local ceramics (Asensio et al., 2016), so the raw ceramics were visually rated to keep the quality consistent. By jaw crushing, those ceramic products were crushed into coarse particles (5-10 mm) (Figure 1b). And they were then dried and ground with an air jet mill to obtain ground CP (Figure 1c).

The ground CP particles show irregular and angular shapes with sharp edges (Figure 2b and c), that resemble cement clinkers (Figure 2a). XRF test showed that silica and alumina occupy the main mass of the oxides in CP (Table 1), and, indeed, they are the dominative components of ceramics worldwide (De Rojas et al., 2018; El-Dieb and Kanaan, 2018; Lavat et al., 2009). CP particle size distribution was measured via a laser particle size analyzer (Beckman Coulter LS 230). As displayed in Figure 2d, most of the CP particles are in micro

Table 2: Mix proportions of the CP-cement mortars.

Sample ID.	Mix proportion (kg/m^3)				Substitution ratio (%)
	Cement	Water	Sand	CP	
Ref.	786	315	1118	0	0
M10	688	306	1118	76	10
M20	596	298	1118	149	20
M30	506	289	1118	217	30
M40	422	281	1118	281	40

sizes below 10 μm with the mean size of 3.5 μm, which are much finer than the cement used in this study. As extensively observed in ceramics wastes elsewhere (Cheng et al., 2016), quartz and mullite are the main crystalline phases of CP (Figure 2e).

A type of quartz sands with the SiO_2 content $> 95\%$ and the fineness modulus of 2.6 was used as the fine aggregates to prepare the mortars.

2.2 Sample preparation

A stepwise graded CP replacing scheme was designed to explore the effect of CP content on the pore structure and transport properties of the CP-cement mortars. A neat OPC mortar with water-to-powder (w/p) ratio of 0.4 (by mass) was designed as the reference. The cement was gradually replaced by CP from 10% to 40% (by mass) with the replacing spacing of 10% under the same w/p ratio. The detailed mix proportions are given in Table 2.

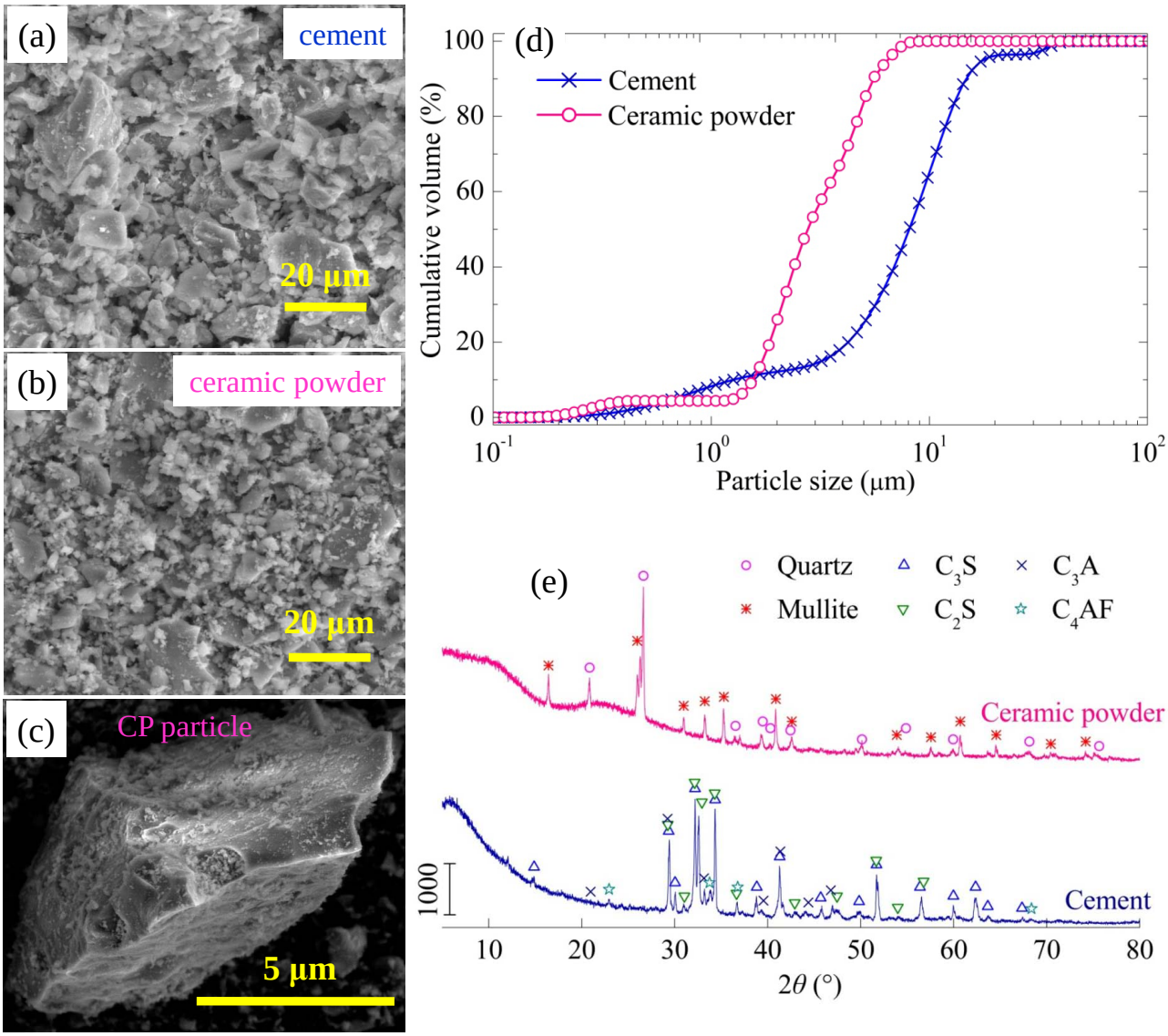

Figure 2: Morphology, mineral components and particle size distributions of the cement and CP: representative SEM images of the cement (a) and CP (b) at the magnification of 3000×; (c) one CP particle at the magnification of 24000×; (d) volume-size distribution curves of the cement and CP; (e) XRD spectra of the CP.

Mortar slurries without obvious material segmentation were obtained via a common mixing scheme. No additives were used to improve mortars' fluidity, while the high contents of CP in cement can slightly cause slump loss. After mixing, mortar slurries were cast in $40 \times 40 \times 160$ mm^3 prism moulds and ϕ 100 $\times$ h 200 mm cylinder moulds. Due to the slow strength gain of mortars with high CP contents, ordinary 1-d curing before demoulding is insufficient to guarantee the quality of the mortar prisms and cylinders. With a primary curing of 3 d (Bentz, 2007; Bentz and Stutzman, 2007; Zeng, 2012), the hardened mortar specimens were demoulded, and then removed in a chamber for water curing with temperature of 20 ℃.

After 180 d curing, specimens were taken out of water for further sample preparation procedures. For WVSI tests, specimens of thin slice are preferred to achieve the equilibrium of relative humidity (RH) between the controlled environment and the specimens as quickly as possible (Li et al., 2018). For each mortar mix, 27 slices of $40 \times 40 \times 5$ mm^3 were sawed out from the prisms. Three cylinders of ϕ 50 mm $\times$ 20–25 mm were drilled out from the cylinders for each mortar to measure durability properties (i.e., gas permeability and capillary sorptivity). The remainders were crushed to particle samples of 2–5 mm for MIP and SEM tests later, and the crushed particles were selected deliberately from the central parts of specimens to avoid the possible material inhomogeneity.

For gravimetry and WVSI tests, the slices were first vacuum-saturated by liquid water and then oven-dried at 50 ℃ to constant weight. For MIP, SEM, gas permeability and capillary sorptivity tests, a 50 ℃ drying operation was performed to obtain the samples with constant weight. Before and after oven-dry procedure, the weight of samples was measured to the accuracy to 0.001 g. The subsequent experiments and their respective sample treatment

procedures are summarized in Table 3.

2.3 Mechanical tests

Mechanical tests were conducted according to a Chinese standard (GB50107-2010). Flexural strength was measured by a machine of WHY-300/10. Before testing, a four-point bending frame with the support span of 100 mm and the loading span of 40 mm was fixed on the loading heads. After a prism specimen was tightly loaded in the frame, forces on the specimen were accumulated in the speed of 50 N/s until it was broken. The recorded maximum forces were applied to calculate the flexural strength.

Three independent runs were conducted for each mix, resulting in six half prisms. These half prisms were then under compression loads in the speed of 2.4 kN/s in the same testing machine. Three datasets of flexural strength and six datasets of compression strength for each mix were averaged to obtain the statistical results.

2.4 Durability tests

2.4.1 Gas permeability

Gas permeability was measured through a CemBureau method with the infiltrating gas of oxygen (Kollek, 1989; Zhou et al., 2012). The principle of CemBureau measurement is to impose constant pressure gradient, measure the gas flow rate in steady state, and evaluate the apparent gas permeability, K_{app} (m^2), through extended Darcy's law for compressible fluids (RILEM TC 116-PCD, 1999). The intrinsic permeability, K_{int} (m^2), is obtained

Table 3: Experiments and sample preparation methods.

Tests	Specimen number	Geometry	Treatment
Compressive/flexural strength	5×3	$40 \times 40 \times 160$ mm	Water-cured to 180 d
Gas permeability	5×3	Cylinders, $\phi 50 \times h$ 20∼25 mm	Water-cured to 180 d, 50 ℃ oven-dried to constant weight
Capillary sorptivity	5×3	Cylinders, $\phi 50 \times h$ 20∼25 mm	The same to gas permeability
MIP, SEM	5×3	Particles, 2∼5 mm	The same to gas permeability
Gravimetry	5×7	Slices, $40 \times 40 \times 5$ mm^3	Water-cured to 180 d, vacuum saturation during 24 h, 50 ℃ oven-dried to constant weight
Water vapor sorption	5×27	Slices, $40 \times 40 \times 5$ mm^3	The same to Gravimetry

through measuring the gas permeability under different pressure gradients and interpreting the pressure-dependent permeability through the Klinkenberg's correction (Klinkenberg, 1941) considering the boundary slip of the gas permeation in pores,

$$K_{\text{app}} = \frac{Q}{A}\frac{2\mu L P_2}{P_1^2 - P_2^2}, K_{\text{app}} = K_{\text{int}}\left(1 + \frac{b}{P_{\text{m}}}\right) \tag{1}$$

in which μ (Pa·s) denotes the dynamic viscosity of infiltrating gas (2.055×10^{-5} Pa·s for oxygen at 20 ℃), Q (m^3/s) is the volumetric flow, L and A stand for the thickness (m) and cross section area (m^2) of the specimen, $P_{1,2}$ (Pa) represent the pressures at the inlet and outlet of permeation cell, P_{m} (Pa) is the average pressure of $P_{1,2}$, and b (Pa) is the Klinkenberg's coefficient.

Three cylindrical specimens were loaded in a CemBureau type permeameter. A constant confining pressure of 7 bars was applied on the specimens to prevent gas leakage and 5 uniform levels of intrusion pressure ranging from 2 to 4 bars were used to enforce oxygen gas to penetrate the specimens (Zhou et al., 2012). Under the action of each intrusion pressure, steady gas flow was recorded once the relative change of volume flow rate Q in successive 10 min was below 1%. And the steady gas flow rate Q was utilized to calculate the apparent gas permeability K_{app} and then fit intrinsic value K_{int} through Eq.(1). Correlation coefficients close to 1 were always observed for the gas permeability tests. One typical regression for intrinsic gas permeability K_{int} is shown in Figure 3(a).

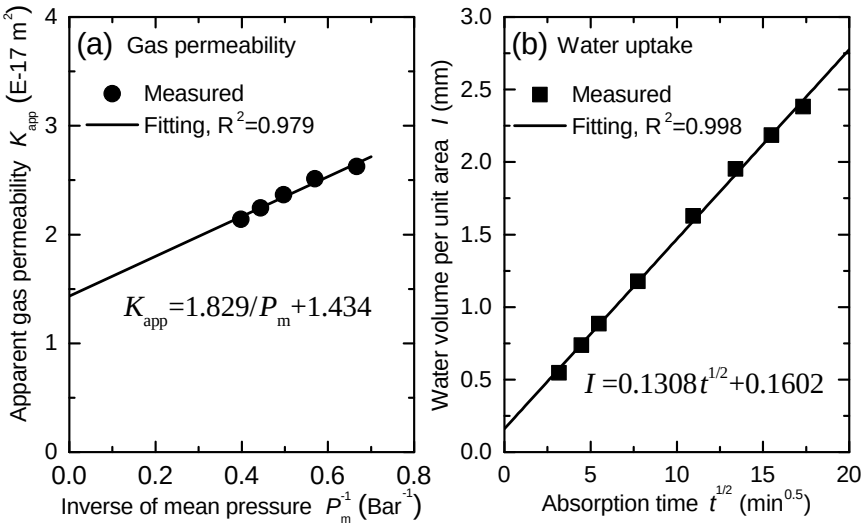

Figure 3: Representative plots of (a) gas permeability against inverse of mean pressure, and (b) water volume absorption per unit area against square root of time (both datasets were from specimen M10).

2.4.2 Capillary sorptivity

Capillary sorptivity refers to the liquid water intake capacity of a porous material through open and connected capillary pores (Esen and Doğan, 2017). The capillary sorptivity can well capture the size, shape and geometry of open pores of the material tested (Sabir et al., 1998; Esen and Doğan, 2018). The specimens for capillary sorptivity were adopted from those after the gas permeability tests. The cylindrical specimens were kept in a water tray with small supports, submerging 2–4 mm only from the bottom of the specimens. The uptakes of water by capillary sorption were measured through the weight gain of the specimen at time intervals of 10, 20, 30, 60, 120, 180, 240, 300 min. At any set time, the specimens were taken out from the water tray, and accurately weighted immediately after the surface water was

removed.

From the measured water sorption weight at different time, the accumulated water suction quantity per unit cross-sectional area I (mm^3/mm^2) is proportional to square root of absorption time t (min),

$$I = S\sqrt{t} \tag{2}$$

where S ($mm^3/mm^2/min^{1/2}$) is the capillary sorptivity coefficient, regressed from the measured $I \sim \sqrt{t}$ curve. One typical plot of capillary sorptivity for a M10 specimen is shown in Figure 3(b). Correlation coefficients approaching 1 ($R^2 > 0.99$) were always held for all water absorption tests.

2.5 Pore structure and microstructure characterization

2.5.1 Gravimetry

Gravimetry method measures the water loss between the saturated and dried specimens, and can evaluate the porosity by the volume ratio between water and specimen. For gravimetry measurements, thin slices, $40 \times 40 \times 5$ mm^3, were vacuum-saturated during 24 h, and the slice volume, V_s, was measured following Archimedes principle. After that, slice specimens were dried to constant weight under 50 ℃. Porosity ϕ_g was calculated by water loss, m_w, and slice volume, V_s,

$$\phi_g = \frac{m_w}{\rho_w V_s} \tag{3}$$

where ρ_w (=1000 kg/m^3) is the density of water. Seven slices of each mortar mix were used to measure the quantities of water loss and slice volume to mitigate the measurement error

induced by material heterogeneity.

2.5.2 MIP

MIP is based on the principle that the intrusion volume of mercury into a porous medium depends on the applied pressure. For cylindrical pores, the pore diameter d_{MIP} can be related to the applied pressure P_{MIP} using Washburn equation,

$$d_{\mathrm{MIP}} = -\frac{4\gamma_{\mathrm{m}}\cos\psi}{P_{\mathrm{MIP}}} \tag{4}$$

where γ_{m} is the surface tension of mercury (0.485 N/m), and ψ is the contact angle between mercury and pore wall (130 °). A volume-weighted pore size distribution (PSD) can be obtained by associating the intruded mercury volume at a given pressure with the pore size evaluated from Eq.(4).

The MIP equipment used in this study is of type Autopore IV 9510 with the intrusion pressure from 3.5 kPa to 414 MPa, corresponding to pore diameter of 356 μm to 3 nm. From the MIP results, the porosity, PSD spectra and other characteristic pore parameters, such as specific surface area (SSA), mean pore size, and threshold pore size, are available for later analysis.

2.5.3 Water vapor sorption isotherm (WVSI)

A parallel method for pore structure characterization used in this work is WVSI. In the WVSI tests, all 27 slices of each mortar would reach a partially saturated condition through RH controls. First, all slices were vacuum-saturated by water and then weighted by an

Table 4: Different RHs created by supersaturated salt solutions (20 ℃)

Salt used	Formula	RH (%)	
		Theoretical	Measured
Deionized water	H_2O	100	99.7
Potassium nitrate	KNO_3	94.6	93.2
Potassium chloride	KCl	85.1	82.6
Sodium chloride	NaCl	75.5	74.4
Sodium bromide	NaBr	59.1	60.4
Potassium carbonate	K_2CO_3	43.2	45.0
Magnesium chloride	$MgCl_2$	33.1	33.3
Potassium acetate	CH_3COOK	23.1	24.4
Lithium chloride	LiCl	11.3	12.0

high accurate electrical balance to obtain their water-saturated mass m_{s}. Then, all slices were oven-dried under 50 ℃ until mass stabilization, and the dried mass m_{d} was recorded. Mass stabilization is reached once the relative mass change is less than 0.1% in 7 days. This equilibrium criterion for drying was always adopted throughout the entire experimental investigation. After that, these 27 slices of each mortar were put three by three into 9 vessels with differently aimed RHs controlled by different supersaturated salt solutions (Table 4). All these 9 vessels were further stored in a closed chamber with temperature controlled as 20 ℃.

RHs in the vessels and mass of the slices were continually monitored. Practical tests

indicated that the measured RHs show slight deviations from the theoretical ones (Table 4). The mositure sorption process took about 29 weeks to approaching the equilibria between the controlled RHs and the surface sorption and/or capillary condensation occurring in the porous CP-cement mortars. After reaching equilibrium, the mass m_{ads} of each partially saturated mortar slice was also obtained.

The adsorption volume w of free water per dry mass of each slice mortar and the water saturation degree Θ during WVSI process can be further determined as,

$$w = \frac{m_{\mathrm{ads}} - m_{\mathrm{d}}}{\rho_{\mathrm{w}} m_{\mathrm{d}}}, \quad \Theta = \frac{m_{\mathrm{ads}} - m_{\mathrm{d}}}{m_{\mathrm{s}} - m_{\mathrm{d}}} \tag{5}$$

The recorded WVSIs provide the relationship between equilibrated water content (or saturation degree) and RH. The sorption isotherms can be further translated into the relationship between Kelvin pore diameter and RH for porous materials. The minimum accessible pore diameter d can be deduced from the controlled ambient RH (h) from the Kelvin equation as,

$$d = d_{\mathrm{K}} + 2\tau, d_{\mathrm{K}} = -\frac{4\gamma_{\mathrm{lg}} V_{\mathrm{mol}}}{RT \ln h} \tag{6}$$

where d_{K}, R (J/mol/K), T (K), V_{mol} (m^3/mol), γ_{lg} (N/m) and τ (nm) are the Kelvin pore diameter, universal gas constant, absolute temperature, molar volume of water and surface tension between water vapor and liquid, thickness of water sorption layers on pore walls respectively.

The thickness of water sorption layers on pore walls depends on the environmental RH. The model by Hagymassy et al. (1969) was adopted and given by:

$$\tau = 0.836h + 0.0626 + \frac{0.0236}{1.015 - h} \quad (\mathrm{nm}) \tag{7}$$

Through Eqs. (6) and (7), one may assess the PSDs of porous materials based on WVSI data.

2.5.4 SEM and EDS

Microstructure of the CP-cement mortars was investigated through a field emission SEM in a device of Quanta FEG650 equipped with an energy-dispersive X-ray spectroscopy (EDS) detector. The collected mortar samples were pre-dried and then manually crushed into smaller pieces (1∼3 mm) to obtain the freshly fractured surfaces. For EDS tests, mortar samples were first impregnated with quick hardening epoxy resin in a cylinder-shaped mould, and then experienced grinding and polishing by various grades of sand-papers and diamond suspensions down to 50 nm. SEM tests were conducted at the accelerating voltages of 20 kV and the working distances of 11 mm. EDS scans were conducted at the voltage of 15 kV and work distance of 16.9 mm.

3 Results and discussion

3.1 Mechanical properties

Figure 4 shows the statistical compressive and flexural strengths of the CP-cement mortars at 180 d. The ultimate compressive strength can be over 80 MPa, and the flexual strength is around 10 MPa. Substituting CP for cement shows no negative impacts on the mechanical behavior of the mortars. For example, the M10 mortar obtained a compressive strength of 86 MPa, which was approximately 7% higher than that of the reference mortar. Jacoby

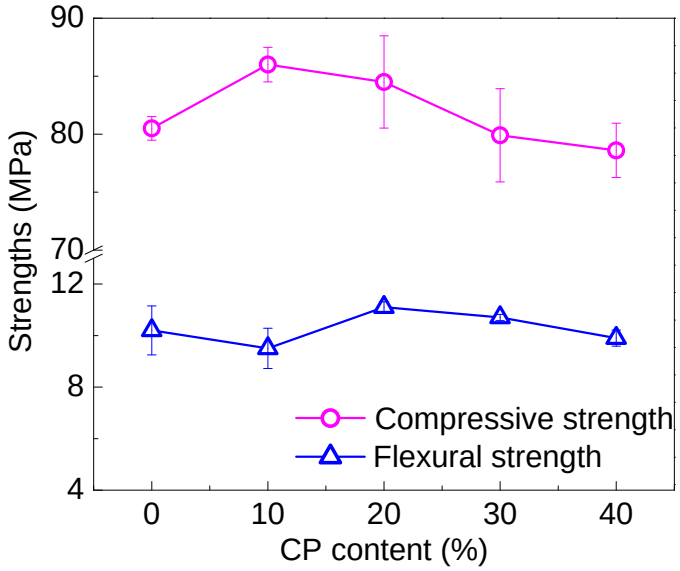

Figure 4: Compressive and flexural strengths of the CP-cement mortars at 180 d.

and Pelisser (2015) and Lasseuguette et al. (2019) also found that the replacement of CP as partial cement can positively enhance the compressive strength of mortars.

The strength enhancement is associated with the chemico-physical properties of CP (Lavat et al., 2009). As a filler, CP can partially fill the gaps and/or voids between cement clinkers, which physically densifies the granular compactness (Huang et al., 2009). In the chemical sense, the pozzolanic reaction of CP generates complex calcium-silicate-alumina-hydrates (C-S-A-H, with Ca/Si ratio $\approx$ 1.0) around the ceramic particles to enhance their interactions with cement hydrates (Li et al., 2020).

3.2 Gas permeability

Figure 5 presents the statistic intrinsic gas permeability for all mortars. The measured intrinsic permeabilities are in the range of 10^{-18} m^2 $\sim$ 10^{-17} m^2. The intrinsic gas permeability

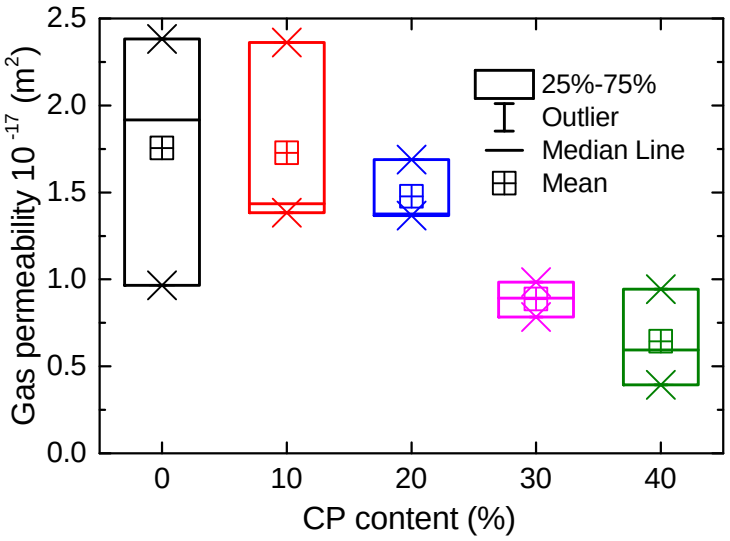

Figure 5: Statistic gas permeability of the CP-cement mortars against CP content.

of the reference mortars is close to the data in literature, e.g. $0.96 \sim 2.60 \times 10^{-17}$ m^2 for mortars with w/p=0.4 by Loosveldt et al. (2002) and $6 \sim 9 \times 10^{-17}$ m^2 for concretes with w/p=0.4 by Gui et al. (2016). Hamami et al. (2012) obtained $K_{\text{int}} = 2.7 \sim 3.4 \times 10^{-18}$ m^2 for their mortars containing 50% limestone powder with w/p=0.4, rather approaching the gas permeability for M40. Thus the obtained K_{int} values have a good agreement with literature data.

As far as gas permeability is concerned, all CP modified mortars perform higher barriers against gas permeation than the reference mortars. For example, the average gas permeability of the neat cement mortars (1.75×10^{-17} m^2) is nearly three times higher than that of the mortars with 40% CP replacement (0.63×10^{-17} m^2) (Figure 5). This is due to the fact that the thin CP particles tend to favor a compact microstructure that may partially seal the interfacial transition zones (ITZs) between aggregates and matrices and narrow the paths for

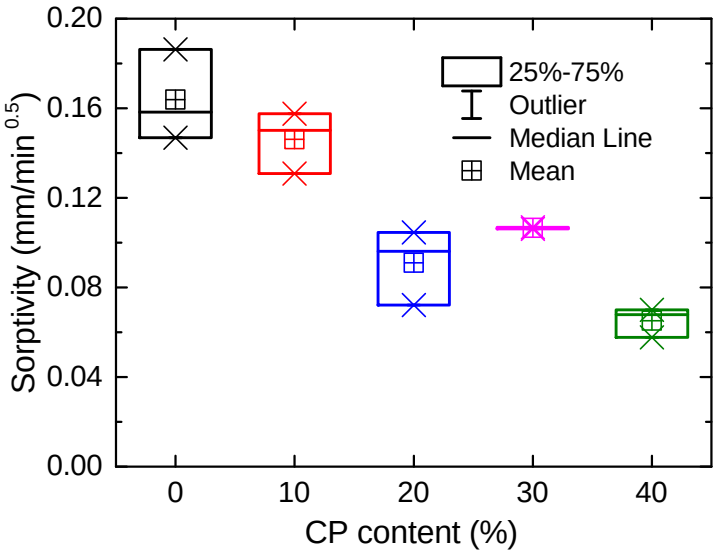

Figure 6: Statistic capillary sorptivity of the CP-cement mortars against CP content.

mass transport (see following subsections for more detailed discussions).

3.3 Capillary sorptivity

Figure 6 displays the statistic capillary sorptivity of all mortars. Considering all mortar types, a rough correlation is observed: mortars having lower gas permeability also have lower capillary sorptivity. Apparently, the neat cement mortars show almost the highest sorptivity, and the presence of CP continually and consistently reduces the sorptivity. The decrease in sorptivity can be greater than 40% when 20% cement is replaced by CP (Figure 6). When the CP replacement ratio increases to 40%, the reduction in water sorptivity can be up to 60%.

This sorptivity decrease, like that of gas permeability (Figure 5), is due to the micro-filler effect produced by the finer particle size of ceramic powder as compared to cement. This

effect results into a dense and compact microstructure and thus inhibits gas permeation and water absorption. Moreover, the possible pozzolanic reactions of CP enhance the homogeneity of mortar matrix (De Rojas et al., 2018), thus resulting in reduced sorptivity. Similar depressions of water sorptivity by incorporation of CP into mortars were reported by Silva et al. (2008).

3.4 Water vapor sorption isotherm

WVSI data averaged over three parallel tests in balance with each RH was collected, and plotted in terms of water sorption volume w per mass of dry mortar (Figure 7(a)) and per 100 g cement (Figure 7(b)). The sorption content (per unit mass of dry mortar) increases slowly and almost in nearly the same rising rate as RH increases to 75%. This slow water rising rate may be attributed the nanostructural units with abundant interlayer spaces calcium-silicate-hydrates (C-S-H) that can accommodate water molecules (Babaee and Castel, 2018). At the higher RH interval, the higher rising rates of the sorption content were observed. The rapid water accumulations may take place in the unfilled spaces among the solid phases, including macro sands, micro fillers (CP in this work) and unhydrated cement clinkers (as well as some micro crystals like calcium hydroxide (CH) and ettringite), and nano hydrates, after cement hydration (Bullard et al., 2011).

The isotherms shown in Figure 7(a) are roughly between the type II and type III isotherms in the category of International Union of Pure and Applied Chemistry (IUPAC) (Thommes et al., 2015). Either isotherm type suggests the existence of macro pores in the tested materials. Due to the lack of data at low RHs ($< 11\%$), the possible occurrences of partial molecular

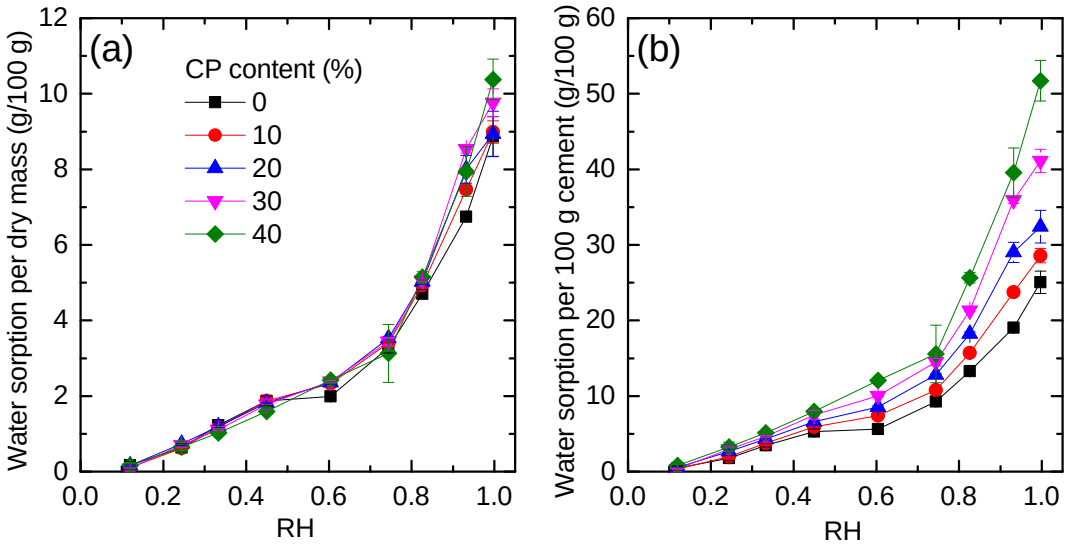

Figure 7: Equilibrium water contents (a) per unit mass of dry mortar and (b) per 100 g cement for the CP-cement mortars at different RH levels in the WVSI experiments.

coverage on pore walls and condensation in micro pores (< 2 nm) cannot be detected from the WVSIs.

Figure 7(a) further depicts that CP has no obvious impact on the isotherm shapes, but the ultimate water sorption content (at RH=0.997) slightly increases as the CP content increases. However, for the plots of liquid saturation degree (Figure 8), incorporation of CP into cement tends to slightly lower down the liquid saturation degree at the same RH level. This means that CP may introduce some large pores beyond the sizes for capillary condensation (at RH=0.997) to store more water. These pores can be some cavities and/or voids generated in the material matrices during mixing and casting due to the reduced fluidity of the mortars with CP.

If one assumes that CP is a non-porous solid, the specific plots of sorption mass with

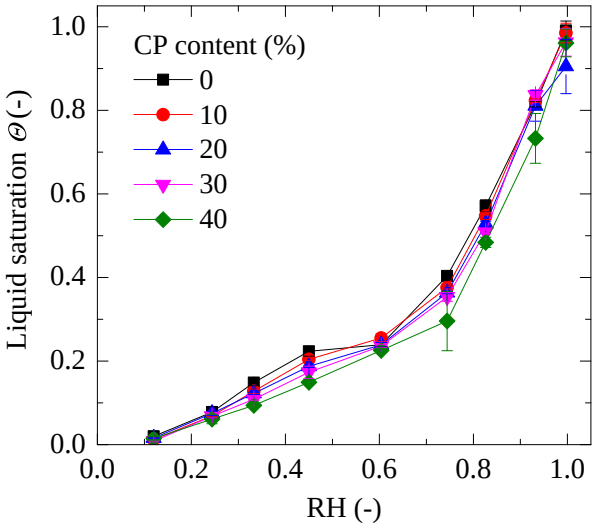

Figure 8: Pore liquid saturations of the CP-cement mortars measured at different RH levels.

respect to 100 g cement may shed some light on specifying the contribution of CP. As displayed in Figure 7(b), the WVSIs of the CP-cement mortars are very close when RH is below 0.33, beyond which the gaps between them become broaden. The fact that the mortar samples have nearly the same WVSIs at low RHs supports the view that C-S-H structures are essentially the same at nano scales for different CP ratios. At high RHs, the corresponding range of pore size shifts to capillary pores, which are intimately related to the CP ratios; see sections below for more profound discussions. The higher CP content induces the larger WVSIs (Figure 7(b)).

3.5 Pore structure analysis

3.5.1 Characteristic pore parameters

Each porosimetry can provide numerous pore parameters that can partially characterize the pore structure of a porous medium, among which the total porosity (ϕ), the threshold pore size (r_c) and the mercury entrapment ratio (α) were concerned in this study. ϕ is relevant to many macro properties of cement-based materials (Boel et al., 2008). r_c corresponds to the mercury percolation threshold for the connected pore clusters in porous media (Katz and Thompson, 1985) and is found to capture the transport properties (Halamickova et al., 1995; Zhou et al., 2017). α denotes how much is the intruded mercury trapped in pores, and may reflect the pore geometries (Zeng et al., 2019).

Figure 9(a) presents the porosity data evaluated from MIP (ϕ_{MIP}) and gravimetric method (ϕ_{g}). Clearly, the MIP porosity ϕ_{MIP} is systematically lower than the gravimetric porosity ϕ_{g} for each mortar ($\phi_{\mathrm{MIP}} \approx 1/2\phi_{\mathrm{g}}$). The difference is owing to the fact that MIP has the limited accessible pore size ($\geq$3 nm in this work), which incapacitates the measurement of thin gel pores below 3 nm, while the gravimetric method does not have such limitation.

The porosity by either test shows clear correlations with CP content and the reference mortar always has the lowest porosity (Figure 9(a)). It seems that the increases in CP content will roughly raise the porosity in a monotonous way. This means that the blend of CP with cement tends to make the material more porous.

However, the threshold pore size (r_c), read from the inflection point on the MIP PSD curves (section 3.5.2), decreases as CP content increases (Figure 9(b)). This implies the

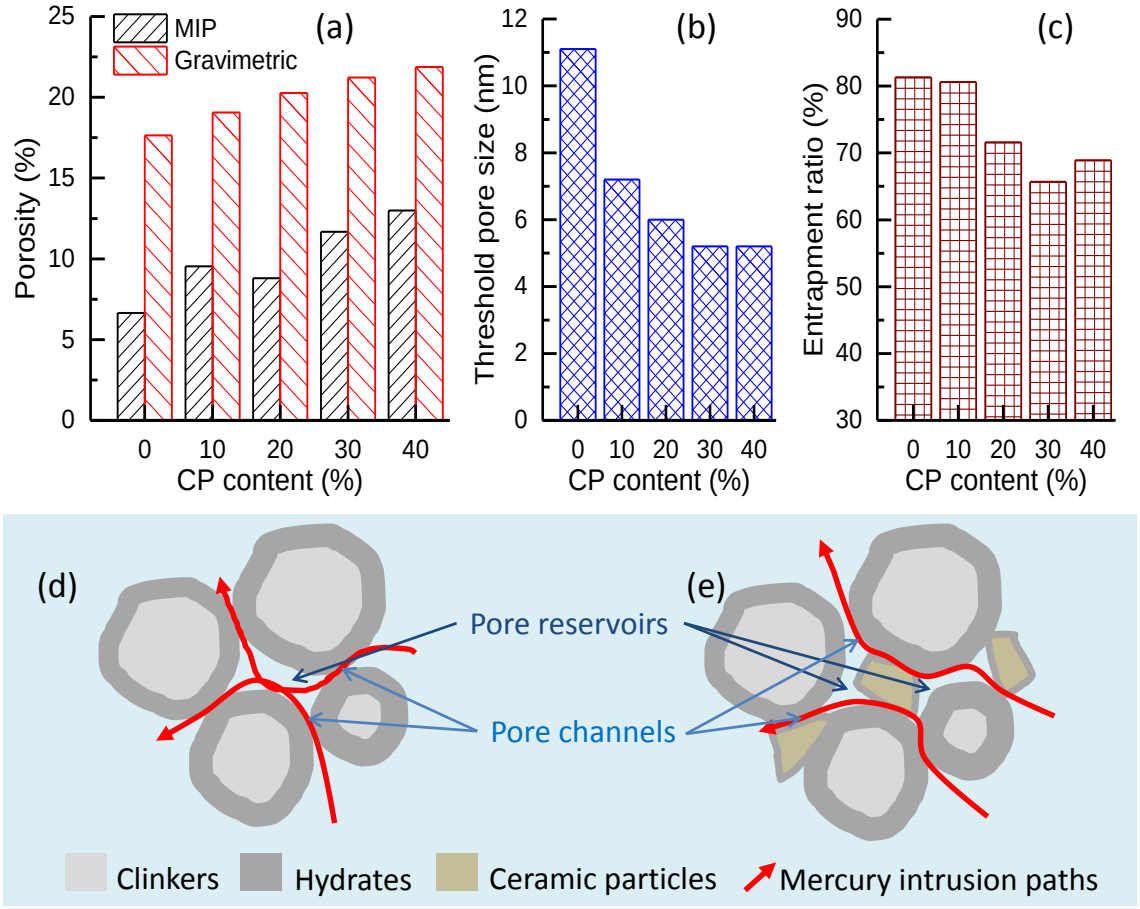

Figure 9: Characteristic pore parameters: (a), total porosity measured by MIP and gravimetric tests, (b), threshold pore size read from MIP, and (c), mercury entrapment ratio. Mechanisms for mercury intrusion through cement materials (d) without and (e) with CP.

promoted resistances against mass transport in the CP-cement mortars. The mercury entrapment ratio α (or the intrusion residual ratio) decreases with CP content as well, telling that the pore geometries are refined by CP.

The changes in total porosity, threshold pore size and mercury entrapment ratio with respect to CP content are the consequences of the physical and chemical impacts of CP on cement matrix and their interplays. For neat cement mortar, the particles assemble together to form relatively big pore reservoirs connected by thin pore channels (Figure 9(d)). The size and geometry of the pore reservoirs and channels are highly depending on the packing patterns of the grains and the filling of the newly formed hydration products (Bullard et al., 2011). When CPs in micro size are incorporated into the clinker packing system, they fill the pore reservoirs and block the pore channels, so both the threshold pore size and mercury entrapment ratio decrease (Figure 9(e)). However, even with the additional pozzolanic reactions of CPs in the cement alkaline environments (De Rojas et al., 2018), the filling and pozzolanic effects can not compensate for the decreases in the binding phases generated by cement hydration when high CP contents are used (e.g., 30% and 40%). In this regime, the total porosity always increases. Similar results were reported elsewhere (Silva et al., 2008; Kulovaná et al., 2016).

3.5.2 Pore size distribution

To gain more insights into pore structure, the PSDs measured by MIP and WVSIs are presented in Figure 10. For MIP tests, mercury rises slowly before it reaches the pores of 30 nm, and then rapidly to the minimum accessible size (3 nm) (see Figure 10(a), where

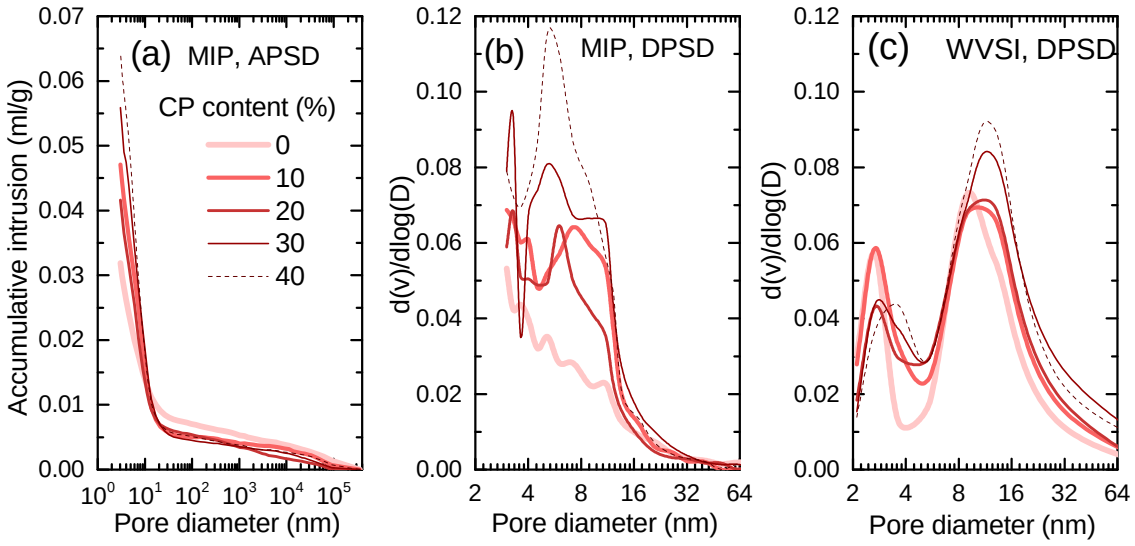

Figure 10: PSDs of the CP-cement mortars tested by MIP and WVSIs: (a) accumulative pore size distributions (APSDs) by MIP, and differential pore size distributions (DPSDs) by (b) MIP and (c) WVSIs.

APSD: accumulative pore size distribution). The first slow rises of mercury accumulation may represent the filling of the superficial irregularities (including the open voids, initial flaws/cracks, cavities and the space between CP and cement grains) on the fractured sample surfaces (Zeng et al., 2019). The second rapid rises of mercury accumulation come from the penetration of mercury fronts into massive capillaries and gel pores under high pressures. More mercury is intruded into the mortars incorporated with more CP (Figure 10(a)).

When gazing at the differential pore size distributions (DPSDs) (Figure 10(b) and (c)), more information about the pore structure alterations by CP can be obtained. Most pores concentrate between 3 and 30 nm for MIP tests and between 2 and 60 nm for WVSI tests. Increasing CP content greatly promotes the intensity of the MIP DPSD spectra (Figure

10(b)). Two peaks appear in the WVSI DPSD spectra (Figure 10(c)): the coarse one between 8 and 30 nm representing the big gel pores and/or thin capillaries, and the thin one between 2 and 4 nm referring to the thin gel pores between C-S-H particles having a bundle (Jennings, 2008) or layer structure (Powers, 1958). Incorporation of CP into cement depresses the thin pore peak intensities but promotes the coarse pore peak intensities (Figure 10(c)).

The obtained pores were further catalogued in three classes: gel pores ($\leq$10 nm), thin capillary pores (10–50 nm) (Aligizaki, 1995) and macro pores (>50 nm) (Thommes et al., 2015), given in Figure 11. Because the limited data of macro pores, only the thin capillaries and gel pores were retained for the WVSI PSDs. The classification of the MIP pore data indicates that as CP content increases, the fraction of the gel pores increases, the fraction of the thin capillaries fluctuates, and the fraction of the macro pores (defined as β for correlation analysis; see section 3.7) decreases (Figure 11(a)). For the WVSI pore segments, in contrast, the fraction of the thin capillaries increases but that of the gel pores decreases with CP increasing (Figure 11(b)).

3.6 SEM and EDS outcomes

Within the theme of this work that concerns about the transport properties of CP-modified cement-based materials, we only focused on the micro morphology of the ITZs between sands and matrix matrices. Figure 12 comparatively and representatively displays the SEM images zoomed in local sands and the neighbouring matrices of the Ref. and M20 mortars in different magnifications. At a first glance, from those pictures, one can hardly observe obvious differences in morphology of the fractured surfaces between the Ref. and M20 (Figure 12(a)

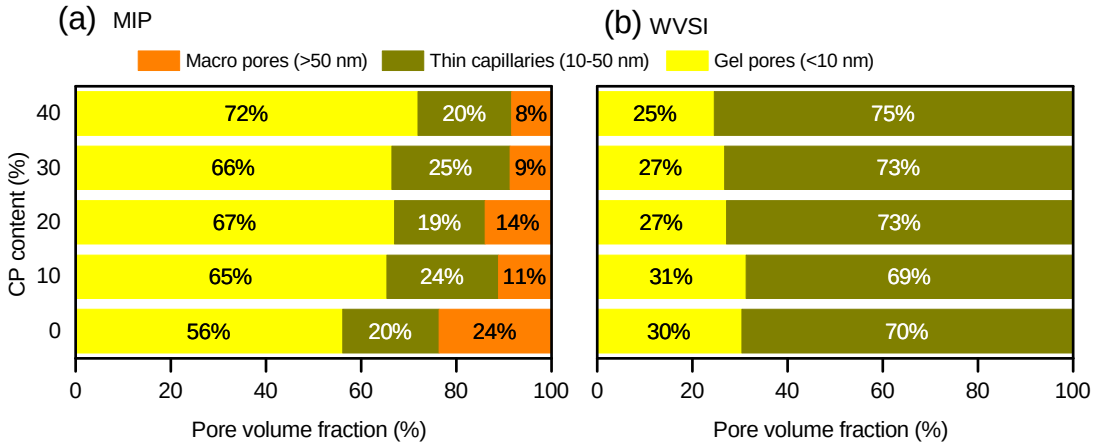

Figure 11: Pore segments from (a) the MIP and (b) the WVSI results. Gel pores ($\leq$10 nm), thin capillary pores (10–50 nm) and macro pores (>50 nm) were classified for the MIP data, and only the former two classes were adopted for the WVSI data.

versus (b)), although CP may change the packing patterns of grains in the mortars (Figure 9(e)).

When carefully examining the SEM pictures, some distinct features of the M20 from the reference mortar can be singled out. First, more crystal-like solids (which are likely to be CH crystals nucleating and growing in the ITZ) appear around the sand in the Ref. sample, while less those solids can be observed in the M20 sample. Second, the fracture surfaces of the M20 sample are much flatter than these of the reference mortar. Third, the matrix-sand contact of the Ref. sample is looser than that of the M20 one (Figure 12(a-1) *versus* (b-1)). Those morphological features suggest that micro CP particles can refine the ITZs between aggregates and cement matrix. The observations are in line with the results documented by Awoyera et al. (2017).

Figure 13 shows the EDS results of a local area in M10 mortar, where only the elements of

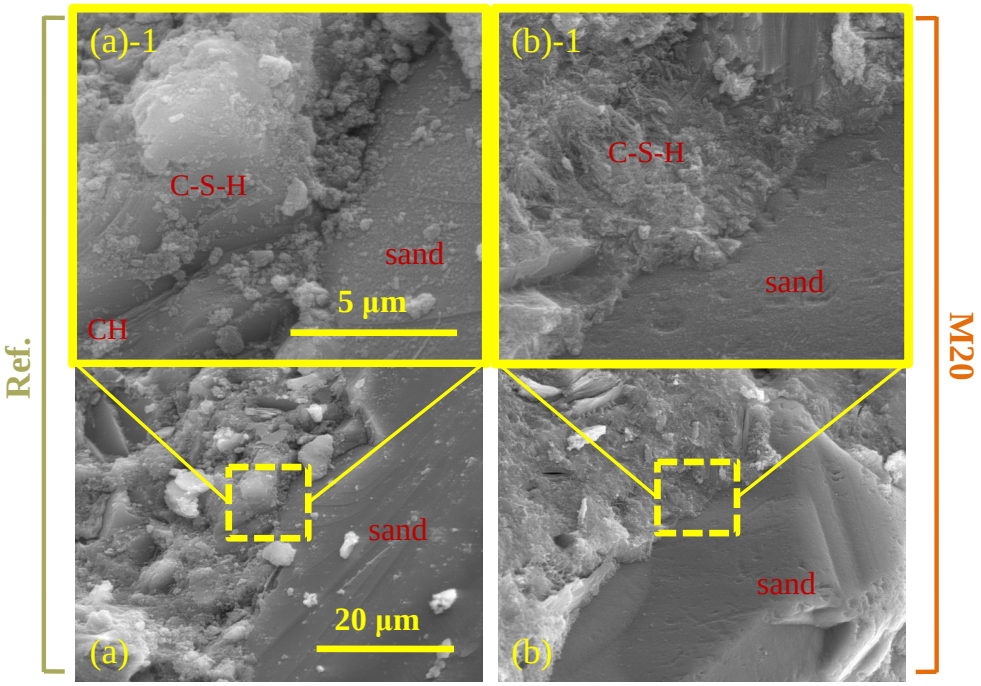

Figure 12: Selected SEM images of pure cement mortar (Ref.) in the magnifications of 5000× (a) and 20000× (a-1); and these of the mortar blended with 20% CP (M20) in the magnifications of 5000× (b) and 20000× (b-1).

Al, Ca and Si were adopted. It is difficult to separate the phases (e.g., sands, CP particles and cement matrix) from an ordinary SEM image (Figure 13(a)). Half of the area is occupied by a sand (quartz) with high intensity of Si, but negligible intensities of Al and Ca. CP particles are mapped with high intensities of Al and Si, but low intensity of Ca. Cement matrix is shown with high intensity of Ca, but relatively low intensity of Al and Si. Those compositional features allow the clear identifications of quartz sand, CP particles and cement hydration in EDS maps (Figure 13(b-d)). Some tiny CP particles may be partially reacted in the alkaline environments of cement matrix, because the Ca intensities around the particles are enhanced, but the Al and Si intensities in the particles are depressed; see the areas in the dashed circles in Figure 13(b-d). The results are in line with those reported by (Li et al., 2020). The coupled effects of ITZ sealing and pozzolanic reaction provided by CPs enhance the durability performances of CP-modified cement materials.

3.7 Correlations between transport properties and pore parameters

Figure 14 describes the dependence of gas permeability K_{int} and capillary sorptivity S on the total porosity $\phi_{\text{MIP,g}}$, threshold pore size r_c and fraction of the macro pores β. Roughly, both the two durability indexes (K_{int} and S) decrease as the total porosity (either ϕ_{MIP} or ϕ_{g}) increases. This is surprisingly contrast to the ordinary observation that durability indexes should increase (if not monotonously and linearly) as total porosity increases (Boel et al., 2008; Civan, 2010; Van den Heede et al., 2010).

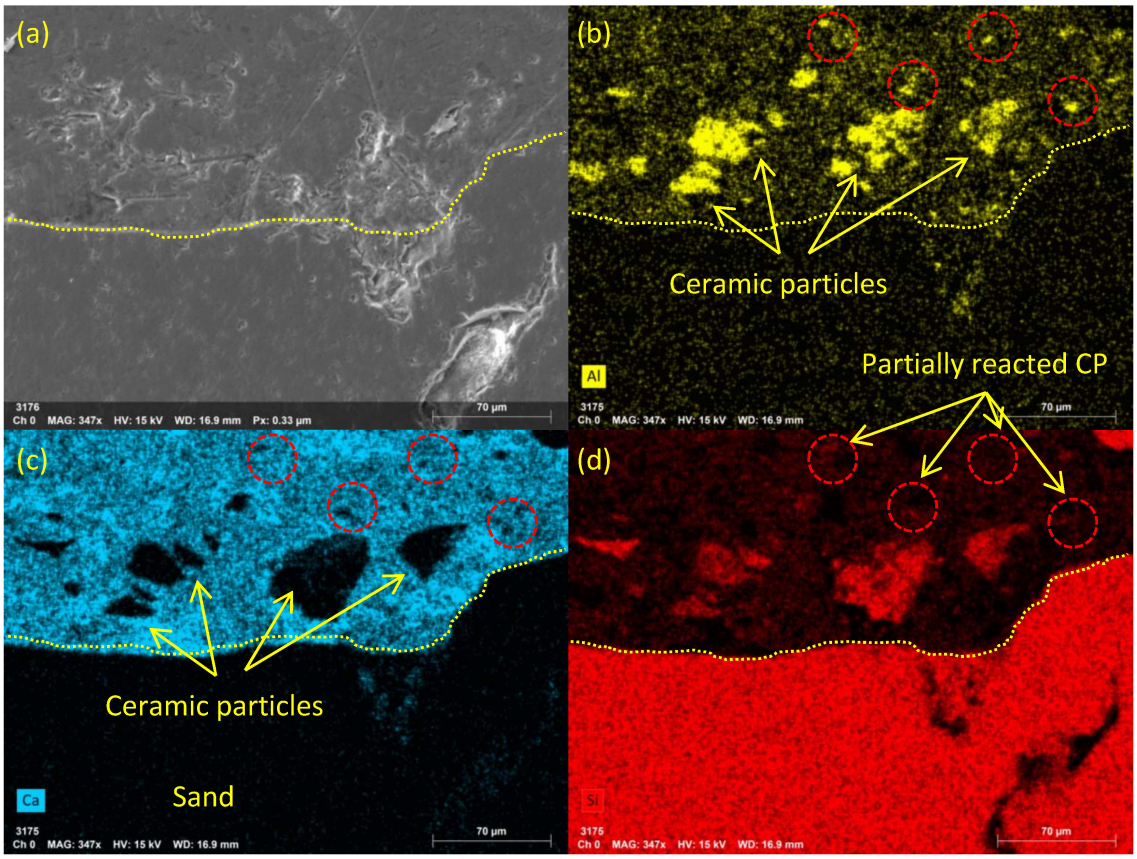

Figure 13: (a) SEM image of a local area in M10 mortar, and the distributions of (b) Al, (c) Ca and (d) Si (The dashed circles indicate the partially reacted tiny CPs).

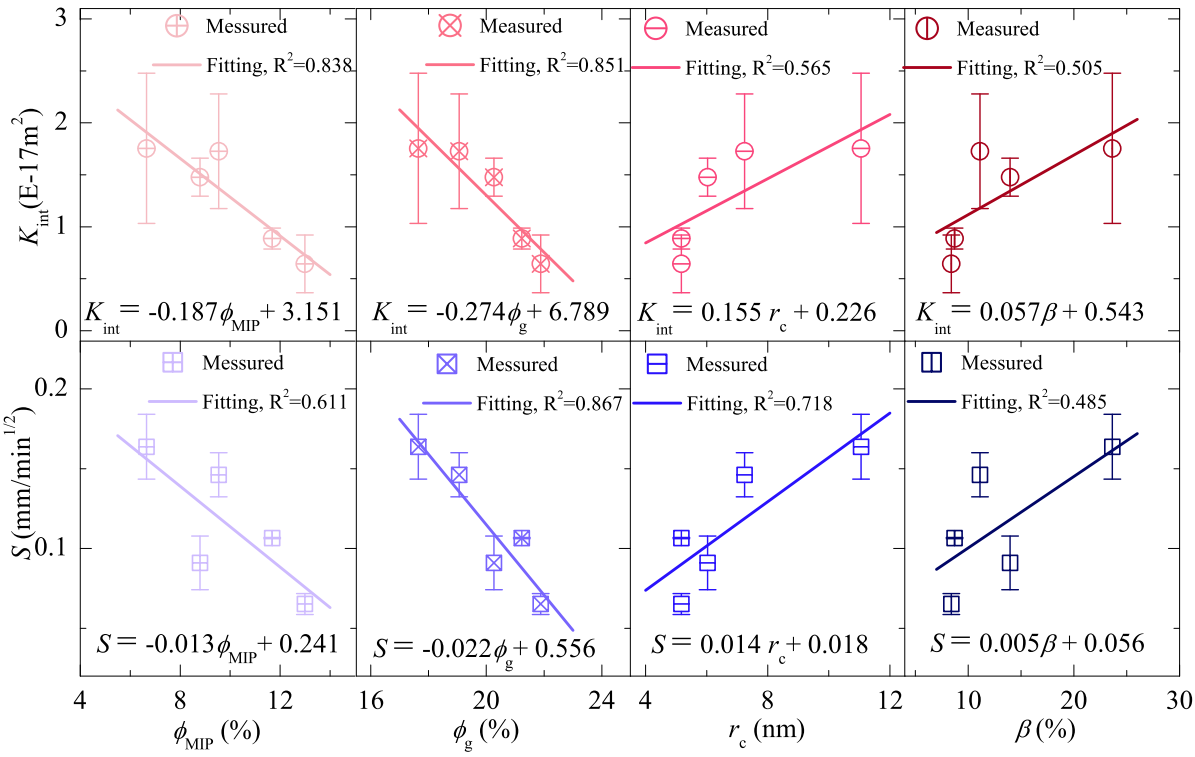

Figure 14: Correlations between the durability indexes (Top half: gas permeability, K_{int}; and bottom half: capillary sorptivity, S) and the characteristic pore parameters (left to right: total porosity by MIP, ϕ_{MIP}; gravimetric total porosity, ϕ_{g}; critical pore size, r_c; and the fraction of the macro pores, β.

To address this paradox, one may go back to think about the relationship between pore volume and its connectivity: Does high pore volume indicate high connectivity? An extreme example may be the foam concrete that generally contains high volume of isolated void but low sorptivity (Nambiar and Ramamurthy, 2007). Although our CP-cement mortars not belong to a foam type, the results displayed in Figure 14 and documented in the literature (Nambiar and Ramamurthy, 2007) imply that total porosity is not the only decisive factor impacting the durability of cement-based materials.

In Figure 14, the correlations between the durability indexes and the threshold pore size r_c (or the fraction of the macro capillaries β) turn back normal: K_{int} and S increase as r_c (or β) increases. Indeed, it was suggested that macro capillary pores (>50 nm) are relevant to the transport processes and detrimental to durability properties of cement composites (Metha and Monterio, 2006). These evidence that pore connection, as well as its threshold size, dominates the transport properties of a porous material. For the CP-cement mortars, the elaborate regulations in physical compactness and chemical reactions of cement and CP jointly refine the pore structure (sections 3.5 and 3.6). As a consequence, both the gas permeability and capillary sorptivity are highly depressed to enhance the barriers to resist mass transport in the CP-cement mortars. However, due to the relatively limited pozzolanic reactions of CP particles, the effect of CPs to strength rises is not as strong as that to permeability improvement.

4 Analysis on economic and durability benefits

Being a waste material, CP is freely available in Jingdezhen. The unit costs of the materials for 1 m^3 concrete, based on local market prices, are indicated in Table 5 for OPC concrete (C40 grade, according to a Chinese standard JGJ55-2011). Costs for 1 m^3 concrete CP-3, SG-3, LF-3 and FA-3 with 30% cement replacement by ceramic powder, slag, limestone filler and fly ash respectively are also given in Table 5. The total cost of 1 m^3 OPC concrete is 49.09 USD. The 30% replacement of cement by ceramic powder, limestone filler and fly ash will decrease the cost to 41.99, 45.61 and 44.19 USD respectively whereas for slag the cost is 50.25 USD. The first three cases indicate a benefit of 14.5%, 7.1%, 10.0% while the SG-3 case incurs a loss of -2.4%. It can be seen that the use of CP in concrete manufacture can gain the lowest material cost without sacrificing the strength.

Durability studies, including gas permeability and water sorptivity, undertaken by researchers related to the inclusions of different powder fillers in concrete are given in Figure 15. The durability reduction index is defined as the reduction of gas permeability/sorptivity with incorporating 1% ceramic powder, slag (Dhir et al., 1996), limestone filler (Marzouki and Lecomte, 2017), fly ash (Gui et al., 2016), waste powder concrete (Ma et al., 2020), marble powder (Mashaly et al., 2016) and glass powder (Schwarz et al., 2008). It can be observed that the incorporation of CP is more beneficial than others by reducing the gas permeability by 1.65%. Partial replacement of cement by CP can result in substantial cost savings with added benefits of reducing the cement consumption and providing better durability.

Table 5: Cost estimation of 1 m^3 OPC concrete and CP-3, SG-3, LF-3, FA-3 concrete (C40 concrete)

Materials	Mix proportion (kg/m^3)					Rate	Total (USD/m^3)				
	OPC	CP-3	SG-3	LF-3	FA-3	(USD/kg)	OPC	CP-3	SG-3	LF-3	FA-3
Cement	430	301	301	301	301	0.070	30.10	21.07	21.07	21.07	21.07
Fine agg.	571	571	571	571	571	0.014	7.994	7.994	7.994	7.994	7.994
Coarse agg.	1213	1213	1213	1213	1213	0.009	10.92	10.92	10.92	10.92	10.92
Water	185	185	185	185	185	0.0004	0.074	0.074	0.074	0.074	0.074
Ceramic powder	0	129	0	0	0	0.015	0	1.935	0	0	0
Slag	0	0	129	0	0	0.079	0	0	10.19	0	0
Limestone filler	0	0	0	129	0	0.043	0	0	0	5.547	0
Fly ash	0	0	0	0	129	0.032	0	0	0	0	4.128
Total cost							49.09	41.99	50.25	45.61	44.19

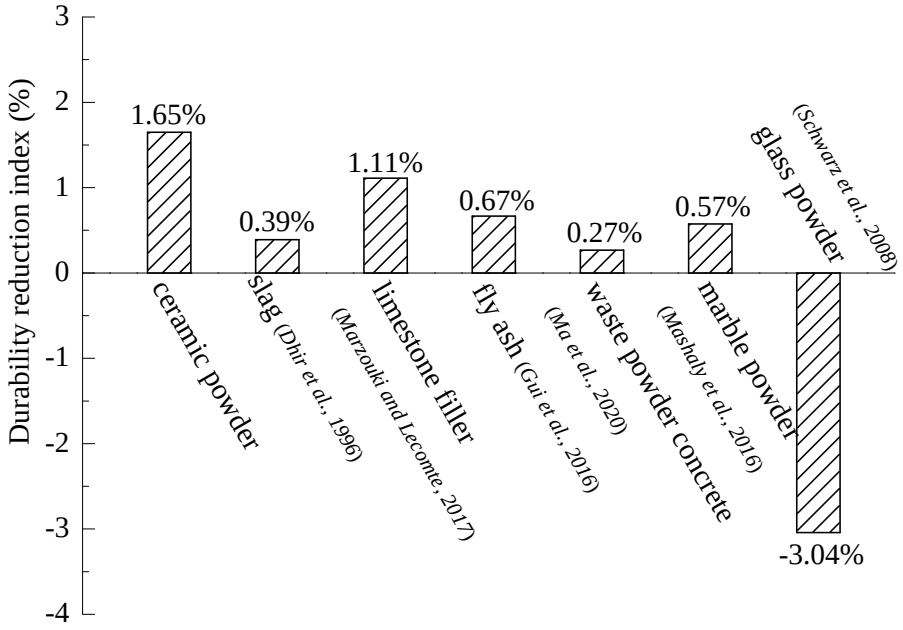

Figure 15: Durability reduction index for concrete with 1% cement replacement by different powder fillers.

5 Conclusions

This study experimentally investigate the mechanical properties, microstructure and transport properties of mortar with various CP content. On the basis of the experimental results, the following conclusions can be obtained.

1. CP can greatly decrease the gas permeability and water sorptivity of mortars. 40% replacement of cement by CP brings the reductions in both gas permeability and water soprtivity by 60%. This suggests that CP can be used as a supplementary material to produce high durable cement-based materials.

2. CP does not change the WVSIs of the mortars, but may induce big pores to slightly

lower down the saturation isotherms. The water sorption contents rise slowly at low RHs $< 75\%$, and then relatively rapidly at high RHs, due to the moisture sorption in different microstructures.

3. CP promotes the total porosity independent of the testing methods. MIP results reveal that increasing CP content decreases the threshold pore size and the mercury entrapment ratio. Pore segments on the MIP data reveal that CP decreases the volume fraction of the macro pores (> 50 nm), keeps the thin capillary pores (10-50 nm) but increase the gel pores (< 10 nm). WVSI pore data suggest that gel pores remain depressed for the CP-cement materials.

4. SEM images and EDS analysis indicate that CP flattens the fracture surfaces, decreases the crystal phases around the sand, and tightens the contact between the matrix and sand. These effects densify the ITZs between aggregates and CP-cement matrix.

5. The gas permeability and water sorptivity inversely decrease with the increasing total porosity, because CP introduce more pores and narrow these pores synchronously. In the same regime, analysis further indicates that gas permeability and water sorptivity increases as the threshold pore size (or the volume fraction of the macro pores) increases.

6. The use of ceramic powder in concrete manufacture can gain better durability and lower material cost. The controls of pore structure and durability indexes enables broad applications of CP for different purposes. Further investigations are needed for better controlling the strength gain and pozzolanic reactions of CP with advanced material characterization.

Acknowledgement

The research is supported by the Natural Science Foundation of China (No. 51808218 and 51878602), Jiangxi NSF project (No. 20171BAB216043) and Jiangxi ED project (No. GJJ170393). We acknowledge Mr. Li Xie in Civil Engineering Department of East China Jiao Tong University and Mr. Yu Peng in Civil Engineering Experiment Center of Zhejiang University for the experiment supports. Le Li would like to acknowledge the financial support of the China Scholarship Council (CSC) under Grant No. 201908360057.

References

Aligizaki, K.K., 1995. Detemination of pore structure parameters in hardened cementitious materials. MS Thesis, The Pennsylvania State University.

Aly, S.T., El-Dieb, A.S., Taha, M.R., 2019. Effect of high-volume ceramic waste powder as partial cement replacement on fresh and compressive strength of self-compacting concrete. J. Mater. Civ. Eng. 31(2), 04018374. https://doi.org/10.1061/(ASCE)MT.1943-5533.0002588

Asensio, E., Medina, C., Frías, M., De Rojas, M.I.S., 2016. Characterization of ceramic-based construction and demolition waste: use as pozzolan in cements. J. Am. Ceram. Soc. 99(12), 4121–4127. http://doi.org/10.1111/jace.14437.

Awoyera, P.O., Dawson, A.R., Thom, N.H., Akinmusuru, J.O., 2017. Suitability of mortars

produced using laterite and ceramic wastes: Mechanical and microscale analysis. Constr. Build. Mater. 148, 195–203. https://doi.org/10.1016/j.conbuildmat.2017.05.031

Babaee, M., Castel, A., 2018. Water vapor sorption isotherms, pore structure, and moisture transport characteristics of alkali-activated and Portland cement-based binders. Cem. Concr. Res. 113, 99–120. https://doi.org/10.1016/j.cemconres.2018.07.006

Bentz, D.P., 2007. Internal curing of high-performance blended cement mortars. ACI Mater. J. 104(4), 408–414.

Bentz, D.P., Stutzman, P.E., 2007. Curing, hydration, and microstructure of cement paste. ACI Mater. J. 103(5), 348–356.

Boel, V., Audenaert, K., De Schutter, G., 2008. Gas permeability and capillary porosity of self-compacting concrete. Mater. Struct. 41(7), 1283–1290. https://doi.org/10.1617/s11527-007-9326-x

Bullard, J.W., Jennings, H.M., Livingston, R.A., Nonat, A., Scherer, G.W., Schweitzer, J.S., Scrivener, K.L., Thomas, J.J., 2011. Mechanisms of cement hydration. Cem. Concr. Res. 41(12), 1208–1223. https://doi.org/10.1016/j.cemconres.2010.09.011

Chen, Z., Wang, H., Ji, R., Liu, L., Cheeseman, C., Wang, X., 2019. Reuse of mineral wool waste and recycled glass in ceramic foams. Ceram. Inter. 45(12), 15057–15064. https://doi.org/10.1016/j.ceramint.2019.04.242

Cheng, Y., Huang, F., Liu, R., Hou, J., Li, G., 2016. Test research on effects of waste ceramic

polishing powder on the permeability resistance of concrete. Mater. Struct. 9(3), 729–738. https://doi.org/10.1617/s11527-015-0533-6

Civan, F., 2010. Effective correlation of apparent gas permeability in tight porous media. Transp. Porous Med. 82(2), 375–384. https://doi.org/10.1007/s11242-009-9432-z.

De Rojas, M.I.S., Frías, M., Sabador, E., Asensio, E., Rivera, J., Medina, C., 2018. Use of ceramic industry milling and glazing waste as an active addition in cement. J. Am. Ceram. Soc. 101, 2028–2037. https://doi.org/10.1111/jace.15355

Dhir, R.K., El-Mohr, M.A.K., Dyer, T.D., 1996. Chloride binding in GGBS concrete. Cem. Concr. Res. 26(12), 1767–1773. https://doi.org/10.1016/S0008-8846(96)00180-9

Dullien, F.A.L., 1992. Porous media: fluid transport and pore structure. Academic Press, San Diego.

El-Dieb, A.S., Kanaan, D.M., 2018. Ceramic waste powder an alternative cement replacement–Characterization and evaluation. Sustain. Mater. Technol. 17, e00063. https://doi.org/10.1016/j.susmat.2018.e00063

Esen, Y., 2010. The effect of cure conditions and temperature changes on the compressive strength of normal and fly ash-added concretes. Inter. J. Phys. Sci. 5(17), 2598–2604. http://www.academicjournals.org/IJPS

Esen, Y., Yilmazer, B., 2010. Investigation of some physical and mechanical properties of concrete produced with barite aggregate. Sci. Res. Essays 5(24), 3826–3833.

Esen, Y., Yilmazer, B., 2011. An investigation of X–ray and radio isotope energy absorption of heavyweight concretes containing barite. Bull. Mater. Sci. 34, 169–175. https://doi.org/10.1007/s12034-011-0028-1

Esen, Y., Orhan, E., 2016. Investigation of the effect on the physical and mechanical properties of the dosage of additive in self-consolidating concrete. KSCE J. Civ. Eng. 20, 2849–2858. https://doi.org/10.1007/s12205-016-0258-2

Esen, Y., Doğan, Z.M., 2018. Investigation of usability of limonite aggregate in heavy-weight concrete production. Prog. Nucl. Energ. 105, 185–193. https://doi.org/10.1016/j.pnucene.2018.01.011.

Esen, Y., Doğan, Z.M., 2017. Evaluation of physical and mechanical characteristics of siderite concrete to be used as heavy-weight concrete. Cem. Concr. Comp. 82, 117–127. https://doi.org/10.1016/j.cemconcomp.2017.05.009.

Geng, Y., Wang, Z., Shen, L., Zhao, J., 2019. Calculating of CO_2 emission factors for Chinese cement production based on inorganic carbon and organic carbon. J. Clean. Prod. 217, 503–509. https://doi.org/10.1016/j.jclepro.2019.01.224

Gui, Q., Qin, M., Li, K., 2016. Gas permeability and electrical conductivity of structural concretes: Impact of pore structure and pore saturation. Cem. Concr. Res. 89, 109–119. https://doi.org/10.1016/j.cemconres.2016.08.009

Hagymassy, J., Brunauer, S., Mikhail, R.S., 1969. Pore structure analysis by water va-

por adsorption: I. t-Curves for water vapor. J. Colloid Interface Sci. 29(3), 485–491. https://doi.org/10.1016/0021-9797(69)90132-5

Halamickova, P., Detwiler, R.J., Bentz, D.P., Garboczi, E.J., 1995. Water permeability and chloride ion diffusion in Portland cement mortars: relationship to sand content and critical pore diameter. Cem. Concr. Res. 25, 790–802. https://doi.org/10.1016/0008-8846(95)00069-O

Hamami, A.A., Turcry, Ph., Aït-Mokhtar, A., 2012. Influence of mix proportions on microstructure and gas permeability of cement pastes and mortars. Cem. Concr. Res. 42(2), 490–498. https://doi.org/10.1016/j.cemconres.2011.11.019

Huang, B., Dong, Q., Burdette, E.G., 2009. Laboratory evaluation of incorporating waste ceramic materials into Portland cement and asphaltic concrete. Constr. Build. Mater. 23(12), 3451–3456. https://doi.org/10.1016/j.conbuildmat.2009.08.024.

Hu, W., Nie, Q., Huang, B., Shu, X., He, Q., 2018. Mechanical and microstructural characterization of geopolymers derived from red mud and fly ashes. J. Clean. Prod. 186, 799–806. https://doi.org/10.1016/j.jclepro.2018.03.086.

Jacoby, P.C., Pelisser, F., 2015. Pozzolanic effect of porcelain polishing residue in Portland cement. J. Clean. Prod. 100, 84–88. http://doi.org/10.1016/j.jclepro.2015.03.096.

Jennings, H.M., 2008. Refinements to colloid model of CSH in cement: CM-II. Cem. Concr. Res. 38(3), 275–289. https://doi.org/10.1016/j.cemconres.2007.10.006

Katz, A.Z., Thompson, A.J., 1985. Quantitative prediction of permeability in porous rock. Phys. Rev. B. 34, 8179–8185. https://doi.org/10.1103/PhysRevB.34.8179

Klinkenberg, L.J., 1941. The permeability of porous media to liquid and gases. Drilling and Production Practice, American Petroleum Institute, New York, pp. 200–213.

Kollek, J.J., 1989. The determination of the permeability of concrete to oxygen by the Cembureau method–a recommendation. Mater. Struct. 22, 225–230. https://doi.org/10.1007/BF02472192

Kulovaná, T., Vejmelková, E., Keppert, M., Rovnaníková, P., Keršner, Z., Černý, R., 2016. Mechanical, durability and hygrothermal properties of concrete produced using Portland cement–ceramic powder blends. Struct. Concr. 17, 105–115. https://doi.org/10.1002/suco.201500029

Lasseuguette, E., Burns, S., Simmons, D., Francis, E., Chai, H.K., Koutsos, V., Huang, Y., 2019. Chemical, microstructural and mechanical properties of ceramic waste blended cementitious systems. J. Clean. Prod. 211, 1228–1238. https://doi.org/10.1016/j.jclepro.2018.11.240.

Lavat, A.E., Trezza, M.A., Poggi, M., 2009. Characterization of ceramic roof tile wastes as pozzolanic admixture. Waste Manage. 29(5), 1666–1674. http://doi.org/10.1016/j.wasman.2008.10.019

Leung, H.Y., Kim, J., Nadeem, A., Jaganathan, J., Anwar, M.P., 2016. Sorptivity of self-

compacting concrete containing fly ash and silica fume. Constr. Build. Mater. 113, 369–375. https://doi.org/10.1016/j.conbuildmat.2016.03.071

Li, L., Li, K., 2015. Permeability of microcracked solids with random crack networks: role of connectivity and opening aperture. Transp. Porous Med. 109, 217–237. https://doi.org/10.1007/s11242-015-0510-0

Li, L., Li, K., 2018. Experimental investigation on transport properties of cement-based materials incorporating 2D crack networks. Transp. Porous Med. 122, 647–671. https://doi.org/10.1007/s11242-018-1019-0

Li, L., Liu, W., You, Q., Chen, M., Zeng, Q., Waste ceramic powder as a pozzolanic supplementary filler of cement for developing sustainable building materials. J. Clean. Prod. 259, 120853. https://doi.org/10.1016/j.jclepro.2020.120853

Loosveldt, H., Lafhaj, Z., Skoczylas, F., 2002. Experimental study of gas and liquid permeability of a mortar. Cem. Concr. Res. 32(9), 1357–1363. https://doi.org/10.1016/S0008-8846(02)00793-7

Ma, Z., Liu, M., Duan, Z., Liang, C., Wu, H., 2020. Effects of active waste powder obtained from C&D waste on the microproperties and water permeability of concrete. J. Clean. Prod. 257, 120518. https://doi.org/10.1016/j.jclepro.2020.120518.

Madlool, N.A., Saidur, R., Hossain, M.S., Rahim, N.A., 2011. A critical review on energy use and savings in the cement industries. Renew. Sustai. Energy Rev. 15(4), 2042–2060. https://doi.org/10.1016/j.rser.2011.01.005

Marzouki, A., Lecomte, A., 2017. Properties of concrete mixed with Portland-limestone cement of different grinding qualities. J. Mater. Civ. Eng. 29(3), 04016241. https://doi.org/10.1061/(ASCE)MT.1943-5533.0001763

Mashaly, A.O., El-Kaliouby, B.A., Shalaby, B.N., El-Gohary, A.M., Rashwan, M.A., 2016. Effects of marble sludge incorporation on the properties of cement composites and concrete paving blocks. J. Clean. Prod. 112(1), 731–741. https://doi.org/10.1016/j.jclepro.2015.07.023.

Mehta, A., Siddique, R., 2018. Sustainable geopolymer concrete using ground granulated blast furnace slag and rice husk ash: Strength and permeability properties. J. Clean. Prod. 205, 49–57. https://doi.org/10.1016/j.jclepro.2018.08.313

Metha, P.K., Monterio, P.J.M., 2006. Concrete, microstructure, properties and materials. McGraw-Hill, London.

Nambiar, E.K.K., Ramamurthy, K., 2007. Sorption characteristics of foam concrete. Cem. Concr. Res. 37(9), 1341–1347. https://doi.org/10.1016/j.cemconres.2007.05.010

Nisbet, M.A., VanGeem, M.G., Gajda, J., Marceau, M.L., 2000. Environmental life cycle inventory of Portland cement concrete. Portland Cement Association, Illinois.

Oggioni, G., Riccardi, R., Toninelli, R., 2011. Eco-efficiency of the world cement industry: A data envelopment analysis. Energ. Policy. 39(5), 2842–2854. https://doi.org/10.1016/j.enpol.2011.02.057

Pacheco-Torgal, F., Jalali, S., 2010. Reusing ceramic wastes in concrete. Constr. Build. Mater. 24(5), 832–838. https://doi.org/10.1016/j.conbuildmat.2009.10.023

Pacheco-Torgal, F., Jalali, S., 2011. Compressive strength and durability properties of ceramic wastes based concrete. Mater. Struct. 44, 155–167. https://doi. org/10.1617/s11527-010-9616-6

Powers, T.C., 1958. Structure and physical properties of hardened Portland cement paste. J. Am. Ceram. Soc. 41(1), 1–6. https://doi.org/10.1111/j.1151-2916.1958.tb13494.x

RILEM TC 116-PCD, 1999. Permeability of concrete as a criterion of its durability, tests for gas permeability of concrete. Mater. Struct. 32, 174–179.

Sabir, B.B., Wild, S., O'Farrell, M., 1998. A water sorptivity test for mortar and concrete. Mater. Struct. 31, 568. https://doi.org/10.1007/BF02481540

Samadi, M., Hussin, M.W., Mohd.Sam, A.R., Lim, H.S., 2015. Effect of ceramic powder on mortar concrete. Adv. Mater. Res. 1113, 62–67. https://doi.org/10.4028/www.scientific.net/AMR.1113.62

Schwarz, N., Cam, H., Neithalath, N., 2008. Influence of a fine glass powder on the durability characteristics of concrete and its comparison to fly ash. Cem. Concr. Compos. 30(6), 486–496. https://doi.org/10.1016/j.cemconcomp.2008.02.001.

Silva, J., De Brito, J., Veiga, R., 2008. Fine ceramics replacing cement in mortars partial replacement of cement with fine ceramics in rendering mortars. Mater. Struct. 41, 1333. https://doi.org/10.1617/s11527-007-9332-z

Singh, M., Choudhary, K., Srivastava, A., Sangwan, K.S., Bhunia, D., 2017. A study on environmental and economic impacts of using waste marble powder in concrete. J. Build. Eng. 13, 87–95. https://doi.org/10.1016/j.jobe.2017.07.009

Song, H.W., Kwon, S.J., 2007. Permeability characteristics of carbonated concrete considering capillary pore structure. Cem. Concr. Res. 37(6), 909–915. https://doi.org/10.1016/j.cemconres.2007.03.011

Tan, L., Yu, F., Chen, X., 2011. Recycling of ceramic wastes as resources. China Ceram. Ind. 18(3), 21–23. (in Chinese). https://doi.org/10.13958/j.cnki.ztcg.2011.03.014

Thommes, M., Kaneko, K., Neimark, A.V., Olivier, J.P., Rodriguez-Reinoso, F., Rouquerol, J., Sing, K.S., 2015. Physisorption of gases, with special reference to the evaluation of surface area and pore size distribution (IUPAC Technical Report). Pure Appl. Chem. 87(9-10), 1051–1069. http://doi.org/10.1515/ci-2016-0119

Van den Heede, P., Gruyaert, E., De Belie, N., 2010. Transport properties of high-volume fly ash concrete: Capillary water sorption, water sorption under vacuum and gas permeability. Cem. Concr. Compos. 32(10), 749–756. https://doi.org/10.1016/j.cemconcomp.2010.08.006

Zeng, Q., 2012. Poromechanics of freezing behavior of cement-based porous materials saturated with salt solution (D.E. thesis). Tsinghua University, Beijing, pp. 76-78. (in Chinese).

Zeng, Q., Wang, X., Yang, P., Wang, J., Zhou, C., 2019. Tracing mercury entrapment in porous cement paste after mercury intrusion test by X-ray computed tomogra-

phy and implications for pore structure characterization. Mater. Charact. 151, 203–215. https://doi.org/10.1016/j.matchar.2019.02.014

Zhang, T., Cai, G., Liu, S., 2018. Reclaimed lignin-stabilized silty soil: undrained shear strength, atterberg limits, and microstructure characteristics. J. Mater. Civ. Eng. 30(11), 04018277. https://doi.org/10.1061/(ASCE)MT.1943-5533.0002492.

Zhou, C.S., Li, K.F., Han, J.G., 2012. Characterizing the effect of compressive damage on transport properties of cracked concretes. Mater. Struct. 45, 381–392. https://doi.org/10.1617/s11527-011-9771-4

Zhou, C., Ren, F., Wang, Z., Chen, W., Wang, W., 2017. Why permeability to water is anomalously lower than that to many other fluids for cement-based material? Cem. Concr. Res. 100, 373–384. https://doi.org/10.1016/j.cemconres.2017.08.002